Nonlinear Dynamics **8:** 213–235, 1995.

A Stochastic Interrogation Method for Experimental Measurements of Global Dynamics and Basin Evolution: Application to a Two-Well Oscillator

J. P. CUSUMANO and B. W. KIMBLE
Department of Engineering Science & Mechanics, Penn State University, University Park, PA 16802, U.S.A.

(Received: 1 October 1993; accepted: 10 May 1994)

Abstract. An experimental study of local and global bifurcations in a driven two-well magneto-mechanical oscillator is presented. A detailed picture of the local bifurcation structure of the system is obtained using an automated bifurcation data acquisition system. Basins of attractions for the system are obtained using a new experimental technique: an ensemble of initial conditions is generated by switching between stochastic and deterministic excitation. Using this stochastic interrogation method, we observe the evolution of basins of attraction in the nonlinear oscillator as the forcing amplitude is increased, and find evidence for homoclinic bifurcation before the onset of chaos. Since the entire transient is collected for each initial condition, the same data can be used to obtain pictures of the flow of points in phase space. Using Liouville's Theorem, we obtain damping estimates by calculating the contraction of volumes under the action of the Poincaré map, and show that they are in good agreement with the results of more conventional damping estimation methods. Finally, the stochastic interrogation data is used to estimate transition probability matrices for finite partitions of the Poincaré section. Using these matrices, the evolution of probability densities can be studied.

Key words: Experimental, bifurcation, homoclinic bifurcation, basin of attraction, probabilistic model.

1. Introduction

The use of bifurcation diagrams and basins of attraction, which summarize, respectively, the local and global stability properties of a system, is now commonplace in nonlinear dynamical analysis. Beyond questions of local stability, a central role in the study of instability phenomena and the onset of chaos is played by the global features of phase space, such as basins of attraction, which are associated with the invariant manifolds of unstable orbits. However, essentially all efforts to visualize and analyze these features have relied on computer simulations: virtually nothing has been done in this area experimentally. In this paper, we present an experimental technique that can be used to obtain basins of attraction for a wide range of physical oscillators. The method is based on the idea of *stochastic interrogation*: an ensemble of initial conditions, which are needed to construct basin images, is generated by switching between stochastic and deterministic excitation.

We apply the technique to a periodically-driven oscillator similar to the well-known two-well magneto-elastic oscillator of Moon and Holmes [1, 2]. A detailed picture of the local bifurcation structure of the system over a specific path in the parameter space is obtained using an automated bifurcation data acquisition system. The evolution of basins of attraction along the same path is studied for forcing amplitudes well below the first period doubling. The transition from simple to complex basin boundaries is observed as the forcing amplitude is increased. Since the entire transient is collected for each initial condition, the same data can be used to obtain pictures of the *flow* of phase space under the action of the Poincaré map.

Dissipation rapidly contracts the phase space, making it possible to obtain an image of the complicated unstable manifolds responsible for chaotic transients, *even when all of the steady state solutions are periodic.*

As a demonstration of how information can be extracted from stochastic interrogation data for practical applications, we obtain damping estimates by calculating the contraction of volumes under the action of the Poincaré map. Using this 'volume logarithmic decrement' data together with the dissipative version of Liouville's Theorem, the damping coefficient is calculated in each well of the oscillator, and shown to be in excellent agreement with coefficients obtained using more conventional methods. This estimate also serves as further validation of the basin data.

A potentially more far-reaching application of the stochastic interrogation technique is to nonlinear modelling. Using only the first iterates of the basin data, we obtain transition probability matrices for finite partitions of the Poincaré section. The result is a global, probabilistic model of the dynamics, which can be used to study the evolution of probability densities in the system.

The experimental apparatus described here is capable of generating automated bifurcation diagrams. A bifurcation diagram is experimentally produced by starting with suitable fixed parameter values and waiting until the system reaches a steady state. Data points are collected (once per forcing period for periodically driven systems) until the steady-state orbit can be determined (current methods limit such measurements to stable solutions only). The parameter values are then slightly incremented, and the process is repeated until the parameter range of interest is investigated. When high resolution is required, manual control of this process can become very time consuming, tedious, and prone to error, especially for mechanical systems operating at low frequencies and possessing long transient times. This is why most experimental bifurcation diagrams found in the literature have been produced using electronic systems, which operate at much higher frequencies [3–5].

Basins of attraction are typically studied using initial condition maps which are derived from Poincaré sections (these are usually limited to two-dimensional surfaces of section). The global stability of an attractor is determined by the size and shape of its basin of attraction, as well as the nature of its basin boundaries. The appearance of fractal basin boundaries can greatly change the transient behavior of a system: long *chaotic transients* can occur after the transition to fractal boundaries [6]. These transients can severely hamper the effectiveness of systems which need short settling times, such as phase-locked loop circuits, in which 'pull-in' times needed to create synchronization become extremely lengthy [7]. The appearance of fractal boundaries greatly increases the final state uncertainty, even for very small initial condition uncertainty [8, 9]. Finally, fractal boundaries can lead to rapid erosion in the size of basins of attraction, severely reducing global stability even when local stability is unchanged [10, 11].

The theory of homoclinic bifurcation furnishes conditions for the existence of complicated invariant sets in the phase space of a dynamical system: in specific applications, necessary (but not sufficient) conditions for the onset of chaos are most often obtained by application of the Holmes–Melnikov perturbation method [12]. It is well understood that the intricate phase-space structures resulting from homoclinic bifurcation do not necessarily give rise to strange attractors: however, homoclinic bifurcation is associated with the phenomena of fractal basin boundaries, fractal–fractal transitions, chaotic transients, and final state uncertainty, even when the possible attractors are all nonchaotic [7–11, 13–17]. It has therefore become one of the major goals of researchers to be able to predict the transition from smooth to fractal boundaries.

In this paper, we offer experimental images of such basin metamorphoses. Thus, our method makes it possible for the first time to experimentally observe homoclinic bifurcations when they occur.

In the next section, the experimental two-well oscillator and the automated data acquisition system are described. In Section 3, the local bifurcation structure of the system is obtained experimentally for a fixed forcing frequency, using the forcing amplitude as the bifurcation parameter. Basins of attraction for the experimental system are presented in Section 4. We present evidence for homoclinic bifurcation in a parameter range in which only two period-1 attractors are apparent in the bifurcation diagram. The evidence consists of a simple-to-complex transition in the basin structure, an increase in the transient time, and the formation of a set containing what is believed to be the complicated unstable manifold predicted by homoclinic bifurcation theory. In Section 5, we show how the basin data can be used to obtain damping estimates for the system using Liouville's theorem. In Section 6, global probabilistic models for the system are obtained and studied by computing transition probability matrices on finite partitions of the Poincaré section. A final discussion and some conclusions are presented in Section 7.

2. The Experimental Setup

The mechanical system for which we find experimental bifurcation diagrams and basins of attraction is a stiffened beam buckled by two magnets. This system is similar to the magneto-elastic oscillator of Moon and Holmes [1, 2]. Moon and Holmes showed that the steady-state behavior of this system is in many respects well-modelled by the two-well Duffing equation, and used the experimental system to demonstrate the physical existence of strange attractors. However, whereas the Moon–Holmes system used a flexible beam, we have added extra stiffness in the form of steel bars (each 19.21 cm $\times$ 0.52 cm $\times$ 1.28 cm) epoxied and bolted along the length of the thin steel beam (20.96 cm $\times$ 0.07 cm $\times$ 1.28 cm), away from the clamped end (see Figure 1). The additional constraint is necessary in our case to force the system to have effectively one degree of freedom even during transients: our method of stochastic interrogation would excite higher modes in a flexible beam making the study of basins of attraction more difficult. A 1.75 cm portion of the beam is left uncovered near the clamped end to act as a hinge from which we are able to determine position using strain gauges. Two rare earth permanent magnets (1.27 cm diameter $\times$ 0.32 cm) are placed on the base of the frame holding the beam to create the two-well potential. The vertical distance between the undeformed beam tip and the magnets is 0.20 cm.

The rigid mount for the system is attached to an electromagnetic shaker which is controlled by the output of a digital-to-analogue (D/A) converter. The signal from the D/A converter first passes through a low pass filter set at 20 Hz, to ensure that higher frequencies caused by D/A conversion are eliminated, and then is amplified before input to the shaker. The strain at the clamp and its time derivative (obtained by analogue differentiation) measure, respectively, the position x and velocity $\mathrm{d}x/\mathrm{d}t$ of the beam. The strain and its time derivative are sent through a low pass elliptical filter set at 50 Hz (thus both signals undergo identical phase shifting). Data was acquired using 12-bit data acquisition (A/D) boards. The ambient system noise signal (output from the filters with the forcing turned off) was found to be on the border of 1 mV rms. Since this is below the resolution of the A/D convertors as scaled for the experiments (2.44 mV for the least significant bit), the noise floor in our measurements was as low as possible with 12-bit digitization.

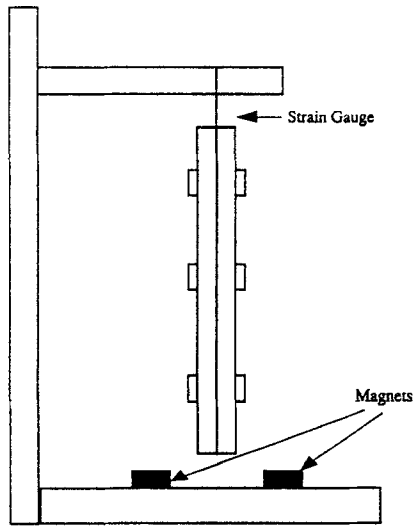

Fig. 1. Schematic of the two-well magneto-mechanical oscillator (see text for dimensions). The constrained beam-magnet system is driven by an electromechanical shaker attached to the rigid frame.

The linear frequency response about the static equilibria of the left and right wells of Figure 1 was obtained using low-level random excitation to verify that the system did indeed have only one degree of freedom. For both equilibria, only one resonant peak was found below 100 Hz: the natural frequencies were found to be 9.14 ± 0.08 Hz for the right well and 9.62 ± 0.08 Hz for the left well. Since the next highest peaks in both transfer functions were about 30 dB down at approximately 225 Hz, we conclude that the system is indeed acting like a single degree of freedom oscillator in the bandwidth of relevance to this study (< 50 Hz). By comparison, using elementary theory for bending vibrations of beams, an unconstrained beam would be expected to have its second natural frequency at about 60 Hz, given a first natural frequency close to those found above.

Data acquisition was carried out with a workstation-based system, and control programs for bifurcation and basin diagrams were written using a library of real-time Fortran subroutines. In addition to the A/D and D/A hardware, the data acquisition system uses a clock board which can be configured with external jumpers to set up the clock cascades needed to synchronize timing and create the burst patterns that trigger sampling at the proper frequencies. This clock-based approach to synchronization is natural for the mechanical system studied in this paper, since the oscillator under consideration is periodically forced, and hence has a natural 'clock'. However, the data acquisition control programs developed for this work are quite general, since interrupts can be presented to our hardware as external clock pulses. For example, should position-based Poincaré sections be needed (instead of the stroboscopic sections used for this paper), simple external triggering circuitry can supply pulses at the appropriate level crossings.

Experimental bifurcation diagrams are obtained in a straightforward manner, although current methods limit us to stable solution branches. The control algorithm outputs a sinusoidal forcing signal with amplitude V, waits a predetermined number of forcing periods for transients to dissipate, and then collects data, again for a predetermined number of periods. The bifurcation parameters are then incremented and the cycle is repeated until the parameter path of interest has been traversed. (For this study, we took the forcing amplitude as our sole bifur-

cation parameter, and the zero-phase stroboscopically-sampled position x of the oscillator as the measure of response amplitude.) The control program has the ability to change direction in the parameter space at a given point. This feature allows branches which have been reached by jumps (as described in the next section) to be explored fully. Thus, given sufficient run time, multiple, coexisting solution branches can be traced out, and hysteretic phenomena can be studied.

Bifurcation and basin diagrams are conceptually complementary: bifurcation diagrams use steady-state data to explore essentially local phase space phenomena (global phenomena are only hinted at indirectly); by contrast, basin diagrams use *transient* data to visualize *global* phase space structures. This complementarity is reflected in the required control strategy, and necessarily makes collecting basin data a bit more complex, since an *ensemble* of transients is required, as opposed to a single steady-state.

The state of our system is given by $(\mathbf{x}, \theta) \in \mathbb{R}^2 \times S^1$ where $\mathbf{x} = (x, \dot{x})$ and the phase $\theta \equiv \omega t \bmod 2\pi$ for a given driving frequency ω. As with the bifurcation diagrams, we take the Poincaré section Σ^{θ_0} to be

$$\Sigma^{\theta_0} = \{(x, \dot{x}, \theta) \mid \theta = \theta_0\}. \tag{1}$$

The dynamics is then completely determined by the action of the period-1 Poincaré map $\phi_T : \Sigma^{\theta_0} \to \Sigma^{\theta_0}$, where $T = 2\pi/\omega$. Typically, basins of attraction are represented by two dimensional images in which the initial conditions in each basin are coded with an identifying color. When numerically generating a basin image (or 'initial condition map'), one discretizes the desired region into finely spaced grid of initial conditions. Then the trajectory of each initial condition is simulated until it has converged to an attractor. In most physical experiments, however, it is very difficult to specify initial data in this manner. Our control program overcomes this problem by using an interval of random excitation to generate a random initial condition $\mathbf{x}_0$ before switching to deterministic forcing. The transient data (i.e. the image of $\mathbf{x}_0$ under repeated application of ϕ_T) needed to discern the asymptotic behavior is collected as soon as the output of the deterministic forcing begins. By repeating this cycle a large number of times, we are able to fill out a portion of the initial condition space near the attractors. Postprocessing of the ensemble of orbits is then done to correlate the initial conditions with the appropriate attractor.

3. Bifurcation Structure of the System

The bifurcation structure of the two-well oscillator for a fixed forcing frequency of 11.009 Hz is shown in Figure 2. It was desired to find a frequency at which the system had a simple basin structure for low forcing amplitudes: preliminary testing with our basin and bifurcation codes indicated that such a situation occurred above 10 Hz (nearer to the natural frequencies, more solutions coexist even at relatively low forcing levels). Two initial branches of solutions were obtained by starting with one initial condition on the left (negative) attractor and one started on the right (positive) attractor, corresponding to small amplitude periodic orbits in each well (left and right are defined by Figure 1, and the sign is given by the vertical scale of Figure 2). For these runs, the amplitude V of the sinusoidal voltage input to the shaker ranged from 0.1 to 1.5 V and back down to 0.1 V, with a step size of 4.88 mV (2 least significant bits). For all the data presented here, 400 periods of data were discarded as transients, and a subsequent 200 samples of the position x as measured by the strain gauge were collected in the zero-phase

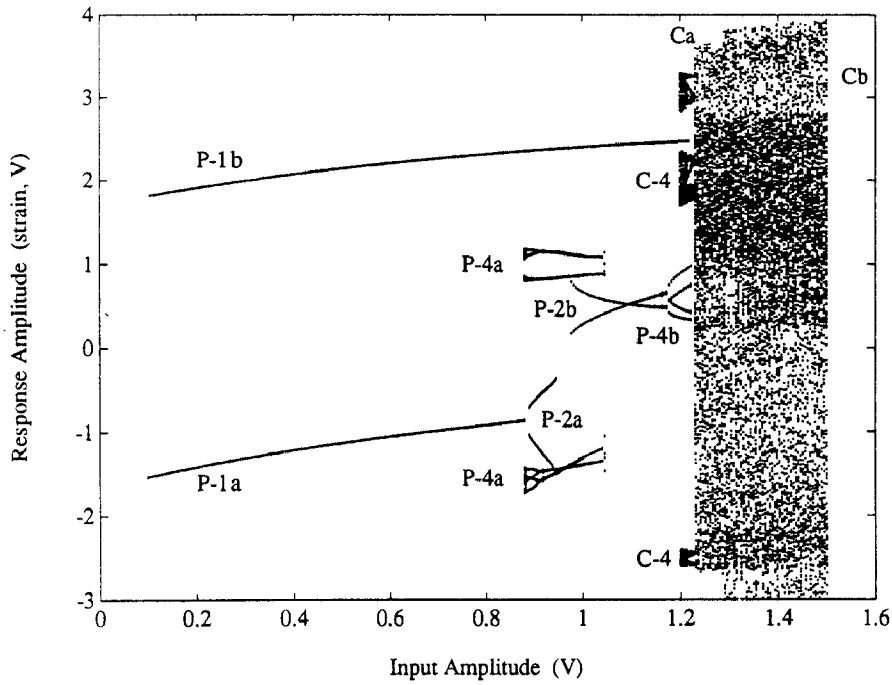

Fig. 2. Experimental bifurcation structure for the system with driving frequency $\omega = 11.009$ Hz. Solution branches are marked with '**P-n**' for period-n orbits, and '**C**' for chaotic orbits.

stroboscopic Poincaré section Σ^0. Typical runs took about 8–16 hours (depending on step size) to scan up and down the entire parameter range.

Certain features of the diagram can *only* be found by backtracking (such as the **P-2b** branch starting with a period-2 saddle-node bifurcation at above 1 V, which we found by backtracking out of the chaotic region). Additional runs were conducted over the ranges of 0.6 to 1.0 V for the negative well and 0.8 V to 1.23 V for the positive well in order to fill out the period-4 branch **P-4a** and the chaotically-modulated period-4 branch **C4** (again, both runs included backtracking). Lowering the voltage step size to the minimum possible with our setup (2.44 mV, or 1 least significant bit) did not change the information in the diagram, although in one case it changed the way in which jumping occurred between the different branches. No other solution branches were found with this procedure, although other disconnected branches may exist: in fact, in the next section we describe a period-3 solution with a very small basin that was found during the basin experiments. If other disconnected branches exist, they too most likely have small basins of attraction.

The left period-1 branch **P-1a** starts at low forcing, and continues with increasing V to 0.881 V, whereupon a period-doubling bifurcation occurs and the branch **P-2a** is created. **P-2a** ends at $V = 0.974$ V, and the response jumps to the period-4 branch **P-4a** (all transitions mentioned here are accurate to 2.44 mV, i.e. 1 least significant bit). Continuing to increase V leads to the end of **P-4a** at $V = 1.047$ V, and the response jumps to the right (positive) period-1 branch **P-1b**. Backtracking on the branch **P-4a** shows that the branch ends at $V = 0.881$ V after period doubling, and the response returns to **P-1a**. To the limit of experimental resolution, the end of the **P-4a** branch coincides with the beginning of **P-2a**.

The branch **P-1b** continues with increasing V to 1.218 V where the response jumps to the chaotically modulated period-4 branch **C4**. By backtracking at this point, the end of **C4**,

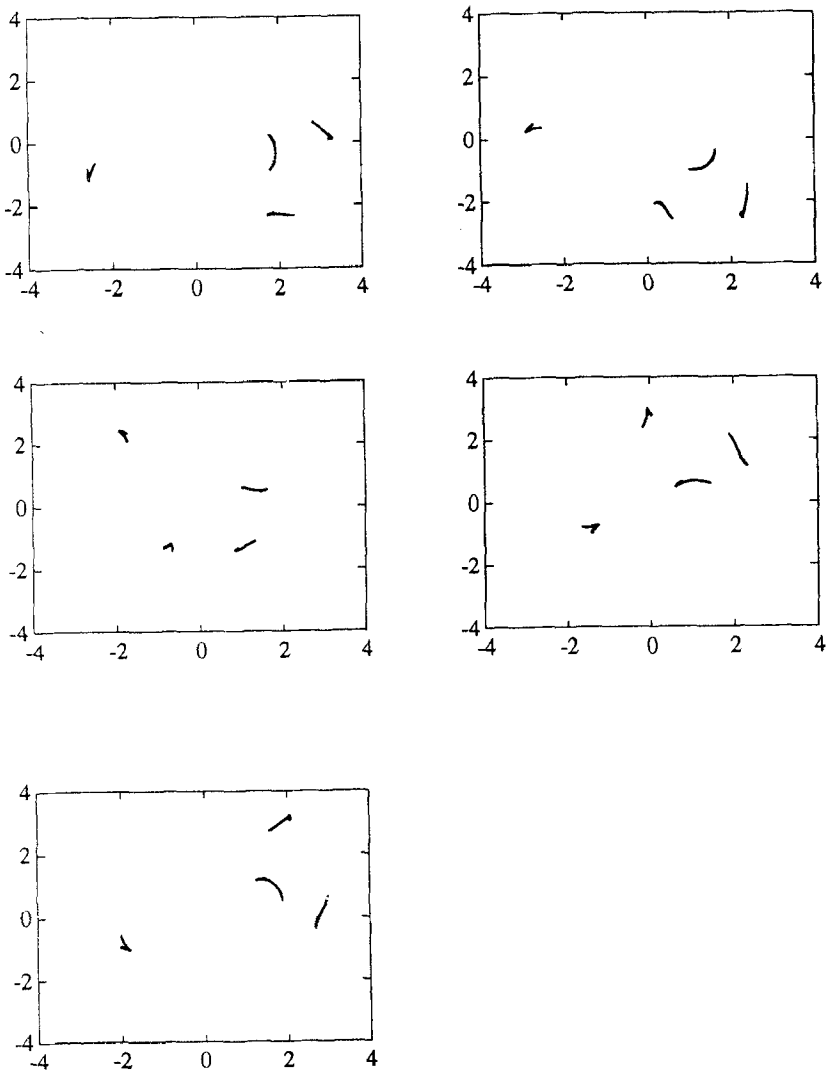

Fig. 3. Poincaré sections for a typical chaotically-modulated period-4 attractor in region **C4** of Figure 2. The phases of the sections are $2n\pi/5$ where $n = 0$ to 4 (read left to right, top to bottom).

at $V = 1.200$ V, is found. In lieu of backtracking, further increases in the voltage along **C4** lead to the sharp transition to the strongly chaotic solutions of **Ca** at $V = 1.232$ V. A final chaotic–chaotic transition occurs at $V = 1.289$ V. Backtracking out of the chaotic region, the response falls on the period-4 branch **P-4b**, which reverse period-doubles at $V = 1.174$ V becoming **P-2b**. Continuing to decrease V leads to the end of **P-2b** at 0.978 V.

Figures 3 and 4 display Poincaré sections of typical chaotic motions in regions **C4** and **Cb**. Correlation dimension estimates [18] were computed using 10^4-point zero-phase Poincaré sections. For the chaotically-modulated period-4 attractor of Figure 3, $d_C = 2.08 \pm 0.03$ over a rather small scaling rage of 3.3 : 1. The more strongly chaotic attractor of Figure 4 has $d_C = 2.68 \pm 0.02$ over a much larger scaling range of over 200 : 1. (The small scaling range for the period-4 chaotic attractor is a consequence of the highly nonuniform distribution of its points in phase space.) Following dimension theory [19], one can conclude that the number of phase space dimensions needed to model the observed chaotic dynamics lies between d_C and

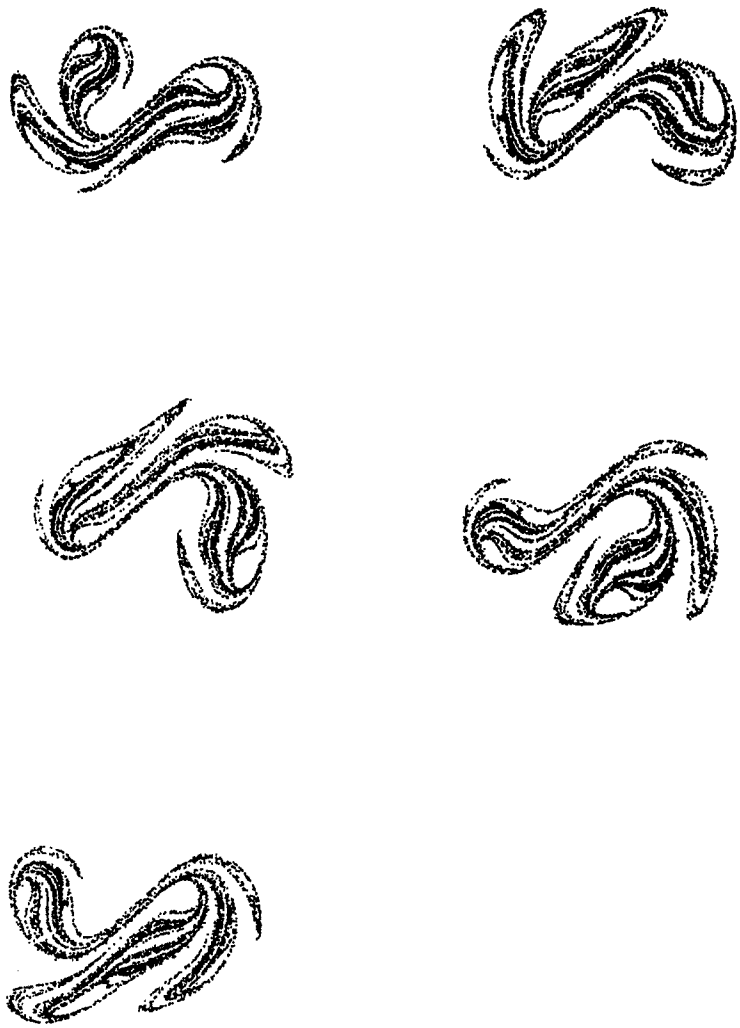

Fig. 4. Poincaré sections for a typical chaotic attractor in region **Cb** of Figure 2. The phases of the sections are as in Figure 3.

next greatest integer to $2d_C + 1$, that is between 3 and 7. Taking into account that the driving phase supplies one state space dimension, this is consistent with (i.e., it does not contradict) the claim in Section 2 that the oscillator essentially has one degree of freedom. Of course, dimension estimates as employed here only furnish information on steady-state motions.

Possibly the most surprising thing about the bifurcation diagram is the large number of jumps between branches and the fact that, though period doubling sequences are observed, the classic period-doubling approach to chaos does not occur. (Our experience to date with various electromechanical systems suggests that this is the norm.) Indeed, the strongly chaotic responses for $V > 1.232$ V occur suddenly, not after an obvious, well-defined, bifurcation sequence. Certainly, one needs to be careful when interpreting these jumps in behavior. Experimental noise and discretization error can cause branch jumping before a solution branch has lost stability if the basin of attraction is too small in some direction. However, in our experiments, we accounted for this possibility by scanning forward and backward over the parameter range of interest multiple times in each run, and by lowering our bifurcation parameter step size until the results stabilized. Thus, experimental data acquisition parameters

are not believed to be the primary cause of the jumps which remain in Figure 2. In at least one case (the beginning of **P-2b** at $V = 0.978$ V), we suspect that the branch starts suddenly from a period-2 saddle-node bifurcation (based on the shape of the branches at that point). However, in general, it is believed that global information concerning the arrangement of coexisting solution branches in phase space is required in order to understand the jump phenomena, sudden branch annihilations, and chaotic–chaotic transitions seen in the bifurcation diagram. A reasonable hypothesis is that some type of crisis [20], in which an attractor collides with another attractor or its basin boundaries, are responsible for at least some of these sharp transitions. To sort this out one would have to correlate the bifurcation results with experimental basin measurements: we leave such an analysis for future work, however a method which could be used to do such studies experimentally is described below.

4. Basins of Attraction and Evidence of Homoclinic Bifurcation

Experimental basins of attraction for the two-well oscillator are presented for 4 runs carried out at a forcing frequency of 11.009 Hz with forcing amplitudes ranging from 0.098 V to 0.498 V. This corresponds to a portion of the simplest part of the bifurcation diagram (Figure 2), in which only two attracting period-1 orbits are apparent. The basin images were each generated in runs consisting of 10^4 stochastic interrogation cycles (i.e. with 10^4 different initial conditions). Each cycle started with the time equivalent of 40 periods of stochastic excitation by digitally-generated, uniformly-distributed pseudorandom noise which was passed through a 20 Hz low-pass filter before being sent to the shaker amplifier. Each run took about 35 hours to complete. The locations of the two period-1 attractors were identified from the data sets. The orbit for each initial condition was then examined to determine its limiting behavior. For definiteness, convergence was defined as having the last iterate in the 50-iterate sample fall within 10 least significant bits (i.e., 24.4 mV) of one of the attractors: points not falling within this neighborhood were labeled 'nonconvergent'. In this way, each initial condition and its subsequent trajectory was identified as belonging to one of the period-1 basins of attraction, or in a set of nonconverging points.

In Figure 5, two-color basin plots for the four runs are shown. In the plots, each initial state $\mathbf{x}_0$ is color-coded according to which periodic orbit $\phi_T^n(\mathbf{x}_0)$ is attracted as n increases. The basin structure clearly undergoes a metamorphosis from simple to complex boundaries as V increases, as evidenced by the increased mixing of colored regions. One suspects that this is, in fact, a transition to fractal basin boundaries, but the resolution of the experiment is not sufficient to unequivocally say this. In principle, one should be able to use the data to estimate the fractal dimensions of the basin boundaries, following [9]. Difficulties associated with the nonuniform distribution of initial conditions and inadequate statistics have, at the time of this writing, hindered successful calculation of this quantity.

More compelling evidence of homoclinic bifurcation can be obtained by exploiting the fact that the stochastic interrogation data allows one to construct images showing the flow of points in the phase space. The basin boundary consists of the stable manifold to a saddle-type orbit: however, sequences of points on the Poincaré section tend to be repelled from this stable manifold. Instead, dissipation in the map tends to push orbits towards the global *unstable* manifold of the saddle-type orbit. A good example of this is in Figure 5(a): a thin ridge of increased density is visible in the center of the figure at a nominal 45° angle with the horizontal, suggesting the location of an unstable manifold emanating from an unstable periodic orbit near $(x, \dot{x}) = (0, 0)$. During the deterministic excitation phase of the interrogation cycle, one can

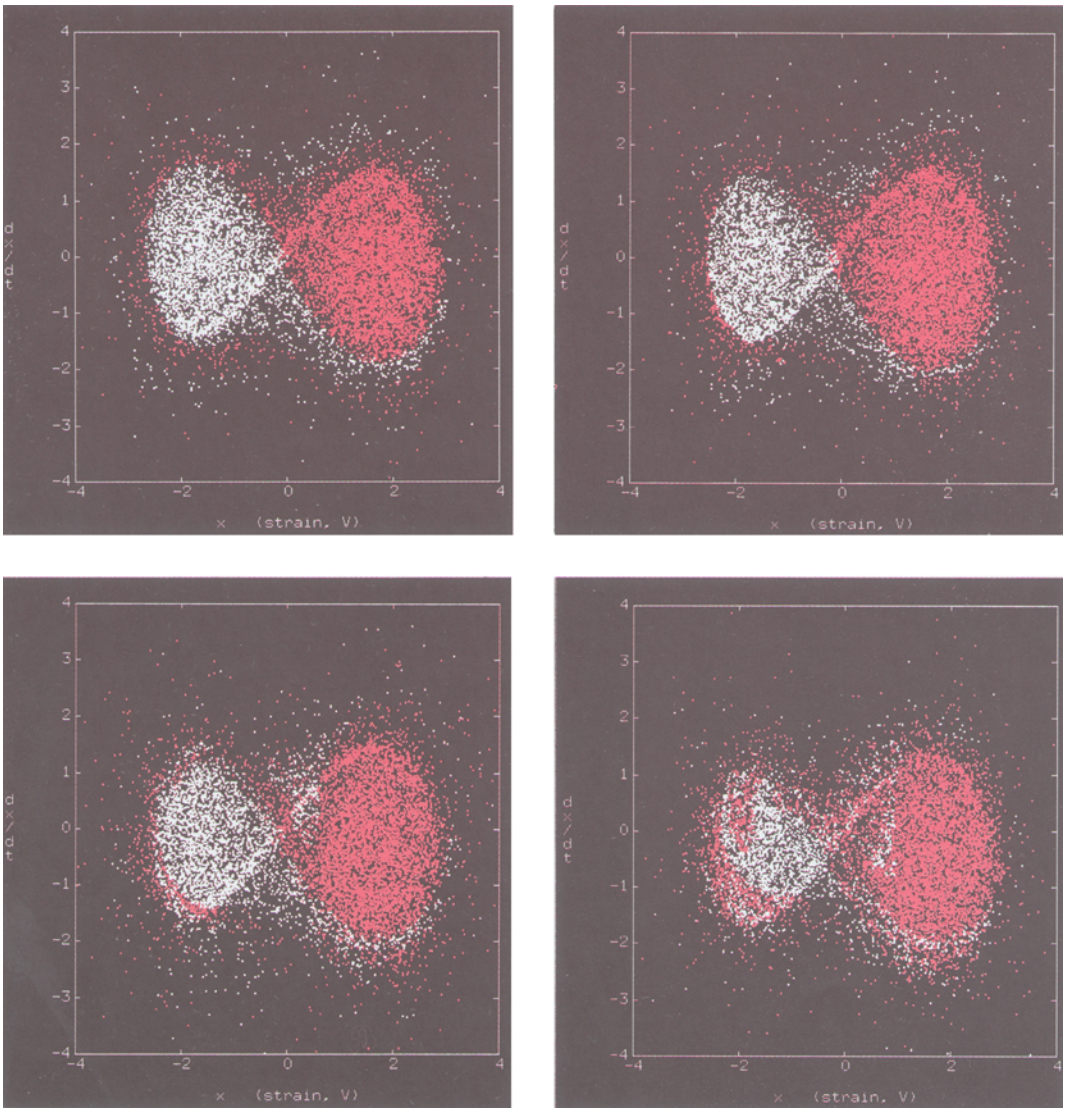

Fig. 5. Experimental basins of attraction with $\omega = 11.009$ Hz: (a) $V = 0.098$ V; (b) $V = 0.198$ V; (c) $V = 0.298$ V; (d) $V = 0.498$ V. Each image consists of 10^4 initial conditions. For all cases, red (resp. white) marks initial conditions which asymptotically approach the right (resp. left) period-1 attractor.

hope to see the approximate location of the unstable manifold near the saddle because of the increased density of points along it, provided the residence time near the saddle is sufficiently long. This situation can be expected to arise precisely when a homoclinic bifurcation occurs: trajectories starting near the saddle will be reinjected there over several forcing periods because of the intersections between the saddle's stable and unstable manifolds.

In Figure 6, the entire ensemble of initial data is shown, along with its image under the action of ϕ_T after 3, 6, and 9 iterates. The variation in point density in the initial conditions (the 0th iterate in each figure) reflects the invariant probability density achieved at the end of the random excitation phase of the interrogation cycle, and hence in each case it is approximately the same. For the lowest forcing level, $V = 0.098$ V the phase space is contracted smoothly

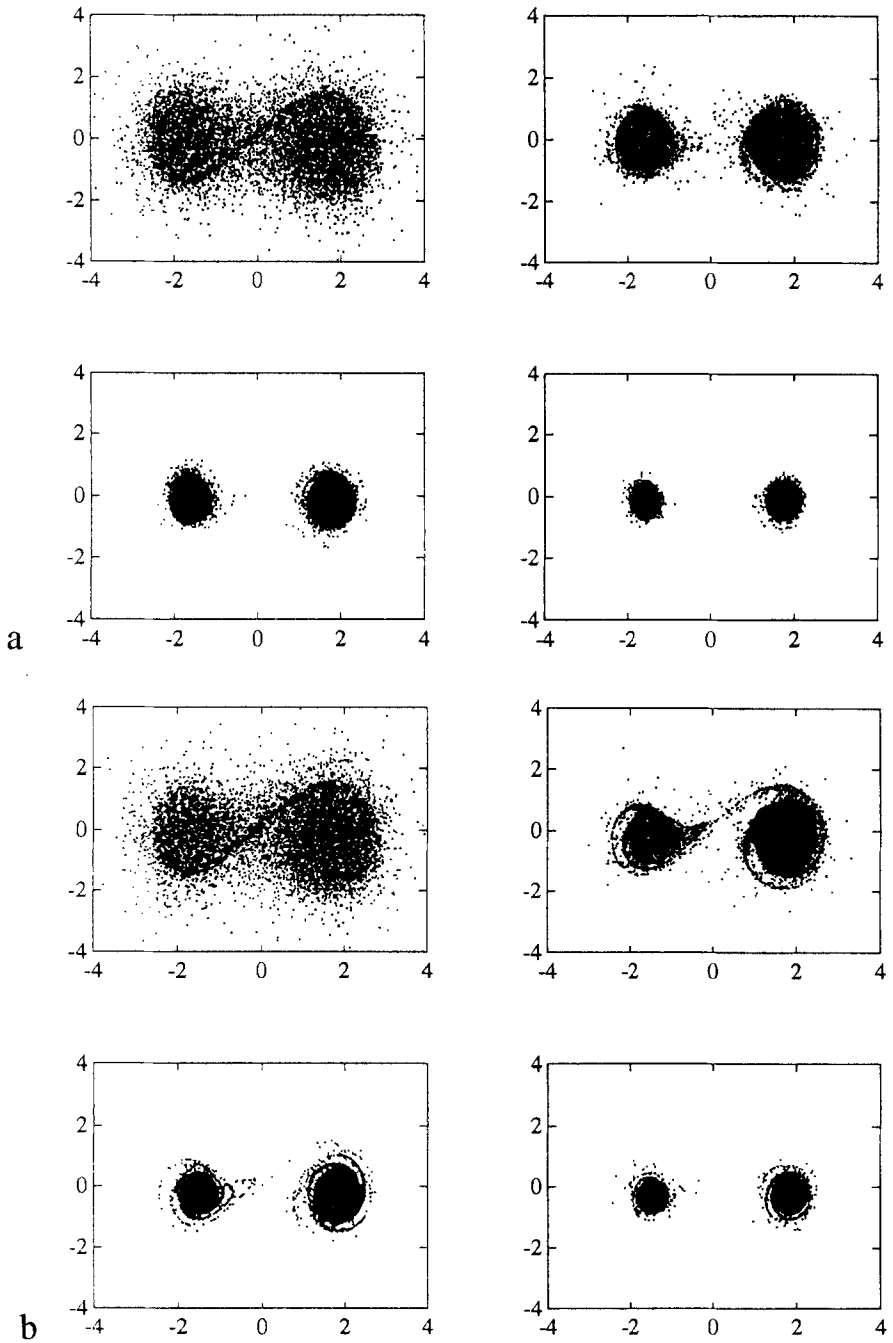

Fig. 6. The flow of solutions on the Poincaré section: (a) $V = 0.098$ V; (b) $V = 0.198$ V; (c) $V = 0.298$ V; (d) $V = 0.498$ V. For each value of the forcing, the image of the ensemble of initial conditions (S), under the nth-iterate of the Poincaré map ($\phi_T^n(S)$) is shown for $n = 0$, 3, 6, and 9 (read left to right, top to bottom). As in Figure 5, $\omega =$ 11.009 Hz.

into roughly circular neighborhoods which collapse down onto the point attractors as the number of iterates increases. In this case, all trajectories starting near the period-1 saddle are rapidly swept towards the period-1 attractors: hence, the unstable manifold near the saddle is essentially invisible after 3 forcing periods.

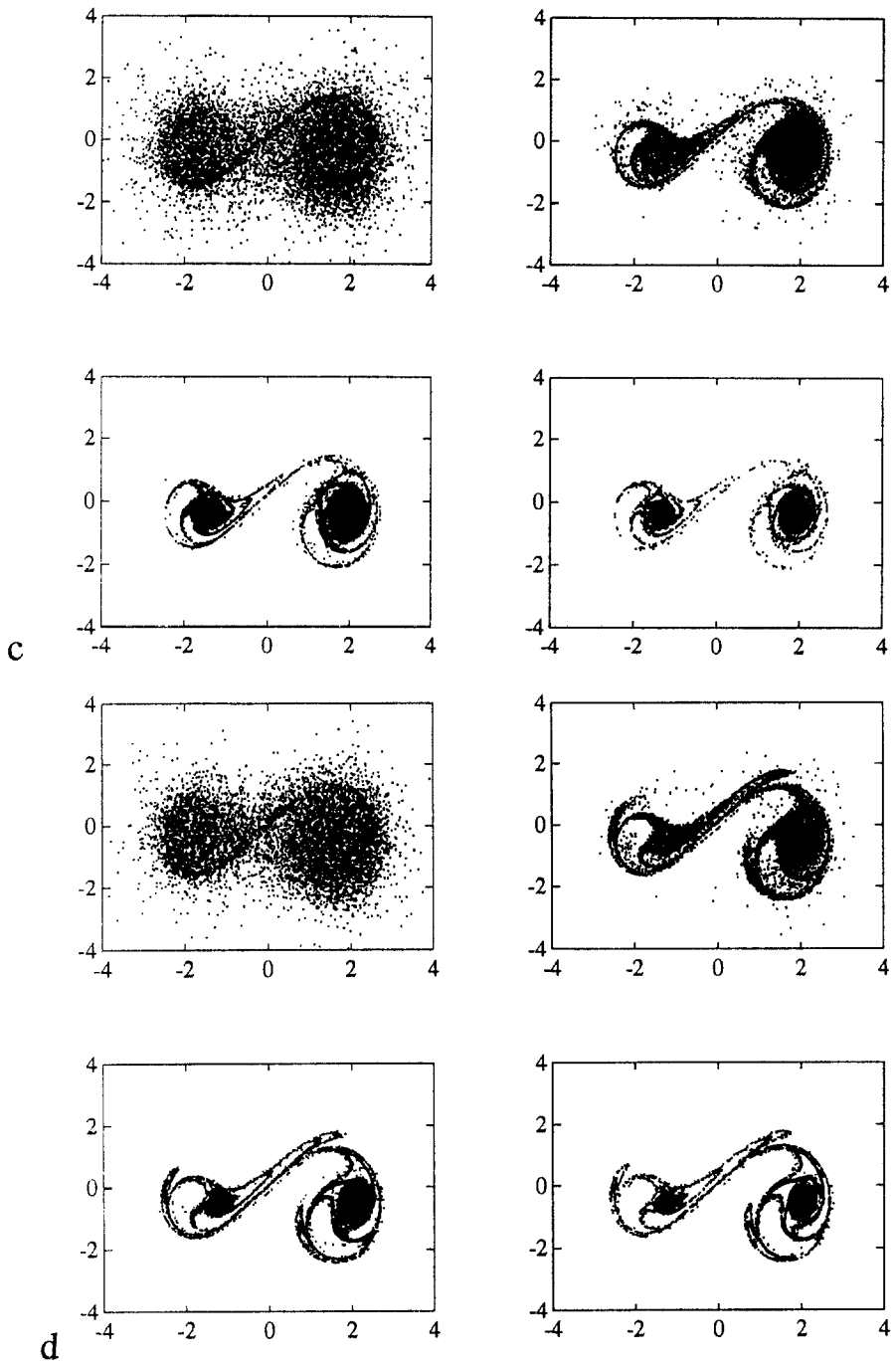

Fig. 6. (c–d)

At higher forcing levels, however, the flow collapses onto a complicated structure in the phase space: we believe that this structure contains the highly folded unstable manifold that one expects to arise near a homoclinic bifurcation. Although such folding is likely to occur before the global bifurcation, it is only *after* the global bifurcation that many orbits with initial conditions near the saddle-type period-1 repeatedly return: hence this structure becomes visible (Figures 6(b–d)). At the highest forcing levels (Figures 6(c–d)), the orbits linger long

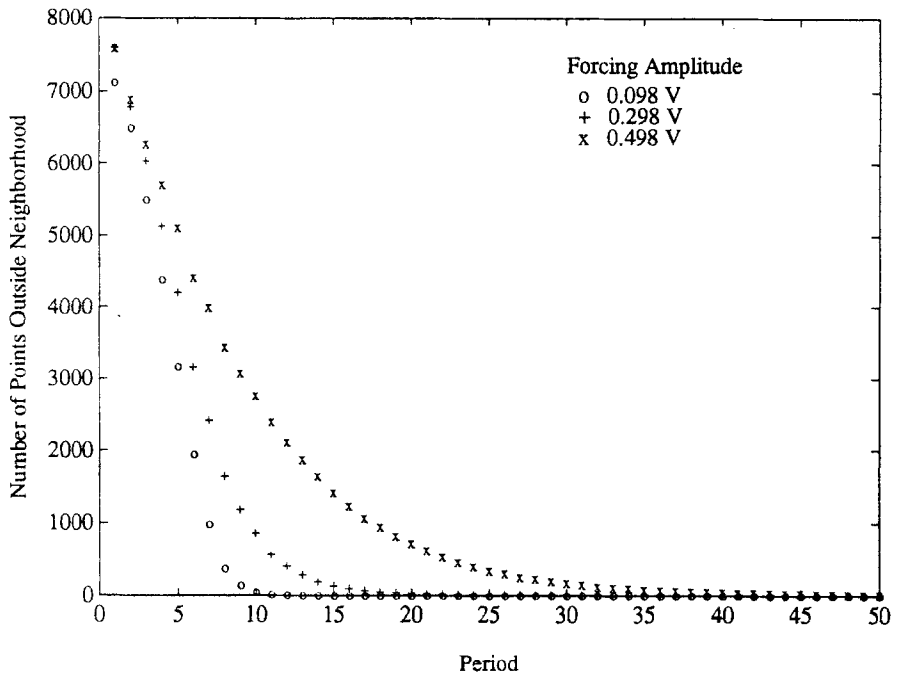

Fig. 7. The number of points remaining outside of a neighborhood of the attractors as a function of the number of iterates (or forcing periods). The neighborhood used for the plots had a radius of 150 least significant bits, or 0.366 V.

enough so that phase space contraction makes the structure look locally very much like a 1-dimensional manifold for several forcing periods, thus revealing the approximate image of the unstable manifold (at least in a region far enough away from the attractors). Note that the unstable manifold can be seen in the flow precisely when the basins begin to lose their simple boundaries (i.e., at $V = 0.198$ V, corresponding to Figures 5(b) and 6(b)).

While at these forcing levels all (except, as explained shortly, for a very small number) of the points eventually approach the period-1 attractors, trajectories starting near the unstable manifold local to the saddle take a long time to escape. In Figure 7, the number of points that remain *outside* of a specified neighborhood of the period-1 attractors is plotted as a function of the number of iterates (forcing periods). All points rapidly enter the neighborhoods in the smooth basin case, but after the loss of smoothness of the basin boundaries (coinciding with the appearance of the unstable manifold structure in the flow data), the number of points staying outside of the neighborhoods at any fixed period rapidly increases.

The homoclinic bifurcation responsible for the metamorphosis in Figures 5 and 6 can be visualized directly by overlaying the basin images with forward iterates of the initial data ensemble. Let S be the ensemble of initial conditions: the image of S under the nth-iterate of the Poincaré map is then $\phi_T^n(S)$. In Figure 8, initial data in the right basin is shown in red, and $\phi_T^n(S)$ is plotted in white, for specific values of n (the iterate used in each plot was chosen to best show the location of the unstable manifold). In Figure 8(a), the approximate location of the unstable manifold is shown by the increased density of white points in $\phi_T^1(S)$ along the diagonal which emanate from the unstable periodic orbit near $(x, \dot{x}) = (0, 0)$ and continue as the boundary of the mass of points accumulating near the period-1 orbits at $(x, \dot{x}) = (1.787, -0.099)$ and $(-1,556, -0.1341)$. In this figure, there is no obvious

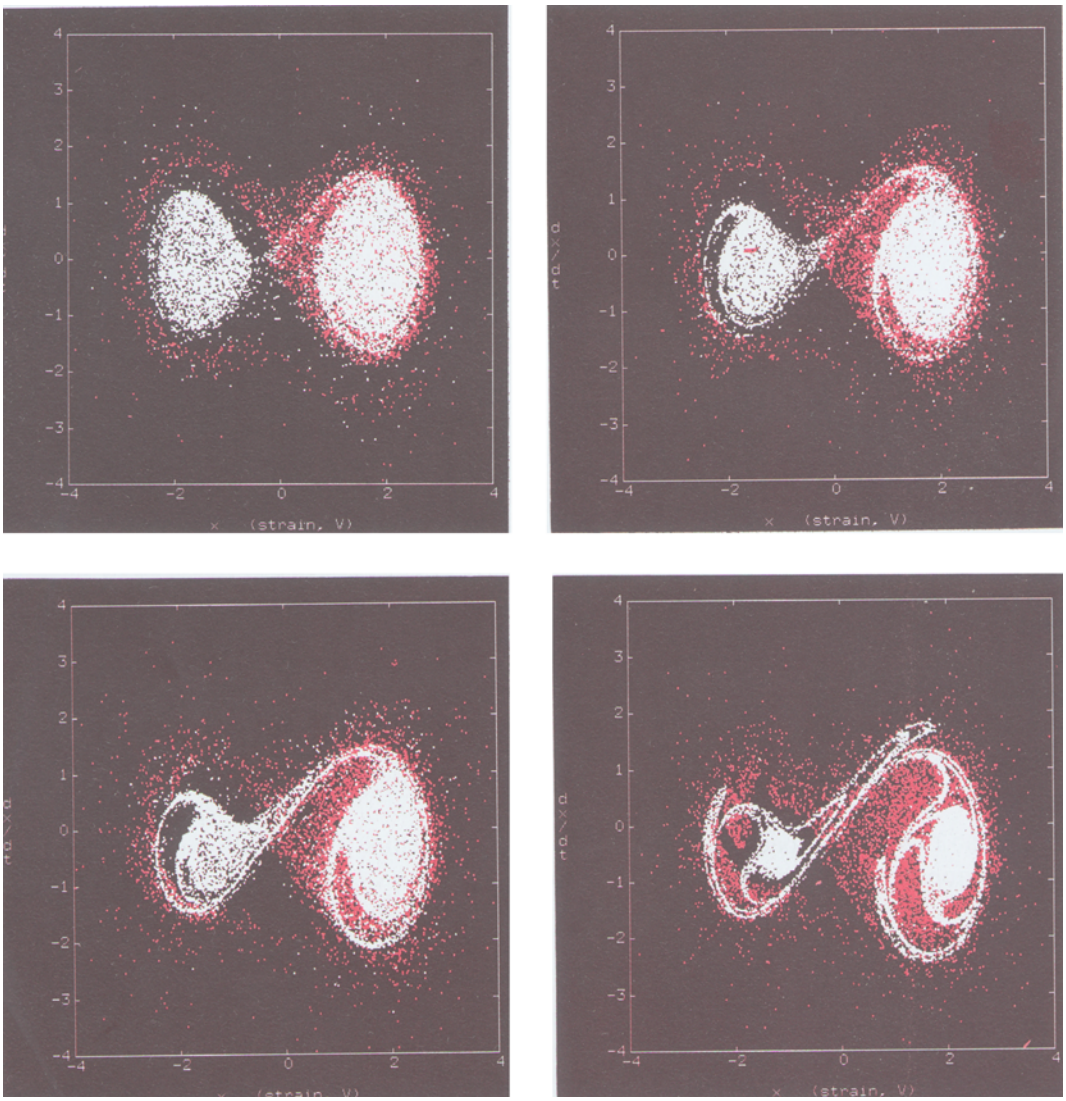

Fig. 8. Overlay plot of the basin data and $\phi_T^n(S)$. The initial data in the right basin is shown in red, and $\phi_T^n(S)$ is plotted in white (the iterate n used in each plot was chosen to best show the location of the unstable manifold). (a) $V = 0.098$, $n = 1$; (b) $V = 0.198$, $n = 3$; (c) $V = 0.298$, $n = 3$; (d) $V = 0.498$, $n = 6$.

intersection between the iterated set and the basin boundary. In Figure 8(b), however $\phi_T^n(S)$ appears to touch the basin boundary (in the left basin), and, at the same time, more internal structure becomes visible in the iterated set. At the higher forcing levels, the crossing is unambiguous (Figures 8(c, d)).

All of this data together leads to the conclusion that a homoclinic bifurcation occurs near $V = 0.198$ V. In addition, these results are consistent with the hypothesis that Figure 5 shows a fractal transition in the basin boundaries. Chaotic transients result from the trapping of trajectories near the global unstable manifold but away from the attractors (as quantified in Figure 7); however, as a practical manner, it is difficult to recognize such behavior by looking at time series unless the transients are unusually long. Even in our worst case, over 94% of

the initial conditions converge to the attractor within 50 forcing periods: in the 4–5 seconds typically available, an observer could easily fail to recognize the system as possessing chaotic transients. Thus, the stochastic interrogation approach to collecting ensembles of data allows this behavior to be seen much closer to the homoclinic tangency.

The number of points classified as nonconvergent after 50 forcing periods was 0, 0, 49 and 593 for V equal to 0.098, 0.198, 0.298, and 0.498, respectively. Examination of the nonconvergent points in the last case revealed a single-well period-3 orbit with a very small basin: only about 74 points, or less than 1% of the initial data, fell within the period-3 basin. The initial conditions in this period-3 basin were very close to the unstable manifold of Figure 6(d), a result consistent with the observations of Grebogi *et al.* in their discussion of accessible boundary orbits.

5. Global Damping Estimates Using Liouville's Theorem

As a simple example of how stochastic interrogation data can be used to characterize the physical properties of a system, we apply Liouville's theorem to the flow of Figure 6(a) and obtain damping estimates.

Liouville's theorem [21], which relates the divergence of the vector field of a system to the rate of contraction of volume elements, is given by:

$$\frac{\mathrm{d}v}{\mathrm{d}t} = \int_v \nabla \cdot \mathbf{f} \mathrm{d}\mu \tag{2}$$

where v is the volume of a region of phase space, and $\mathbf{f}$ is the governing vector field. We assume, as would be the case for the two-well Duffing oscillator with linear damping, that the system equations have the form:

$$\begin{aligned} \dot{x} &= y \\ \dot{y} &= -2\zeta y - g(x) + F\cos\Omega t \end{aligned} \tag{3}$$

where ζ is the critical damping ratio, and the relative driving frequency $\Omega = \omega/\omega_0$ for a given natural frequency ω_0 (time has been rescaled by ω_0 for convenience). The divergence of the time-dependent vector field $\mathbf{f}$ (the right hand side of equation (3)) is then easily found to be

$$\nabla \cdot \mathbf{f} = -2\zeta, \tag{4}$$

which is a constant. Thus, equation (2) becomes

$$\frac{\mathrm{d}v}{\mathrm{d}t} = -2\zeta v, \tag{5}$$

which yields

$$\ln\frac{v}{v_0} = -2\zeta(t - t_0). \tag{6}$$

Since the basin data evolves under the action of ϕ_T, it is natural to take $t - t_0 = T$ and define the *volume logarithmic decrement* δ_v as

$$\delta_v \equiv \ln\frac{v}{v_0} = -2\zeta T. \tag{7}$$

Table 1. Comparison of critical damping ratios estimated using the volume logarithmic decrement on the forced system, with the standard amplitude logarithmic decrement estimate for free vibrations.

Forcing frequency (Hz)	Forcing amplitude (V)	right well	left well
11.009	0.098	0.022 ± 0.003	0.020 ± 0.004
11.009	0.198	0.022 ± 0.003	0.021 ± 0.004
9.105	0.098	0.024 ± 0.005	0.02 ± 0.01
9.404	0.098	0.024 ± 0.003	0.002 ± 0.004
free vibration		0.023 ± 0.001	0.021 ± 0.001

Rearranging equation (7) gives the following relationship between the critical damping ratio ζ and δ_v:

$$\zeta = \frac{-4\pi\delta_v}{\Omega} . \tag{8}$$

In elementary vibration theory, the equivalent formula relating the *amplitude* logarithmic decrement δ_x [22] to the critical damping ratio is

$$\zeta = \frac{-\delta_x}{2\pi} , \tag{9}$$

where the change in amplitude is defined as taking place over one period of *free* vibration.

Definitions (8) and (9) are both used to estimate the damping coefficient. Figure 9(a) shows a semi-log plot of basin 'volume' (area) versus forcing period of each cycle for the right (positive) attractor of the system with parameters as in Figures 5(a), 6(a) and 8(a). The area of the region occupied by the ensemble of points in the right basin of Figure 5(a) was estimated at each period by multiplying the standard deviations in the x and $\mathrm{d}x/\mathrm{d}t$ directions. This is not a very good area estimate initially, but becomes quite good as the points cluster around the attractor, and yields a nice scaling region until the points are all contracted into the noise of the measurements (after about 40–45 periods). The slope of the fitted line is an estimate of δ_v. Similarly, Figure 9(b) shows a semi-log plot of vibration amplitude versus number of periods for a free vibration about the right potential well. The slope of the fitted line in this case is the amplitude logarithmic decrement δ_x. The resulting damping coefficient estimates for this and other trials are shown in Table 1. We remark that study of the amplitude logarithmic decrement data produced from the free vibration time series showed that the damping for the system is approximately piecewise linear, depending on the size of the oscillation. Therefore, to compare damping estimates from the two methods, only free oscillations comparable in amplitude to those used to find δ_v from the basin data were used to estimate δ_x. With this in mind, the damping estimates based on Liouville's Theorem and the volume decrement are in very close agreement with those obtained using the more conventional method.

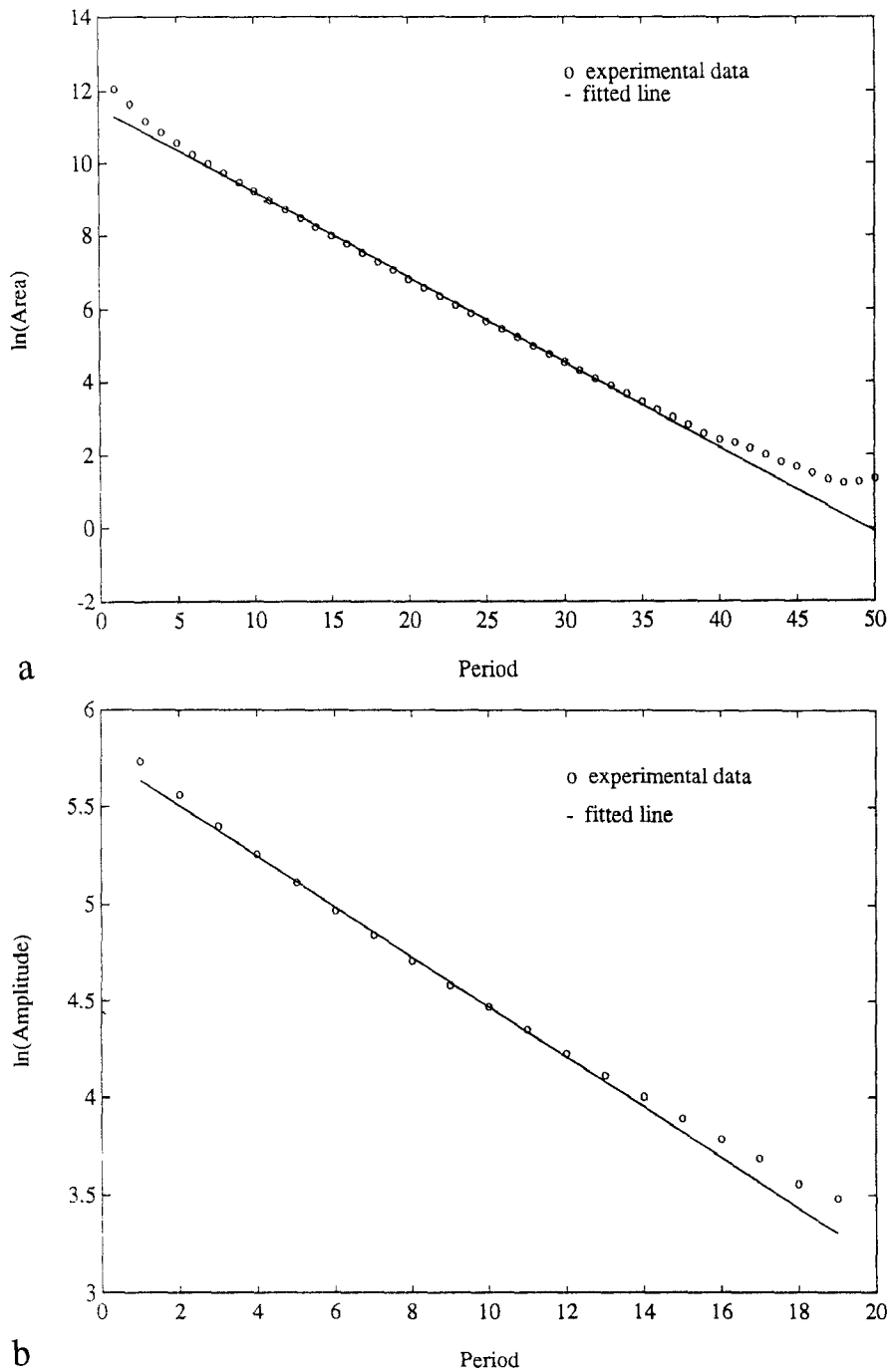

Fig. 9. Comparison of volume logarithmic decrement data (a) for the forced system to amplitude logarithmic decrement data (b) for free vibrations. Both data sets are for the right attractor with ω = 11.009 Hz and V = 0.098 V. The slope of the fitted line gives δ_v for the top plot and δ_x for the bottom plot. See Table 1.

6. Nonlinear Probabilistic Modelling

We now demonstrate how the stochastic interrogation data can be used to construct transition probability matrices for finite partitions of the phase space. These matrices allow the evolution

of probability densities to be studied [23, 24]. In general, quantities such as the entropy of the Poincaré map, the invariant distribution for the system, and basins of attraction, can be estimated. A detailed study of such experimentally-determined probabilistic models will be presented elsewhere: for this paper, we limit ourselves to describing perhaps the simplest construction of such transition probability matrices, and showing their effect on a uniform initial density of states. We remark that the experimental approach taken here is similar to the generalized cell mapping numerical method developed by Hsu [25], with perhaps the main practical difference being that the data used to define P_{ji} is not uniformly distributed in our case.

To compute the transition probability matrices, we partition the phase space of our system into M^2 boxes using an $M \times M$ grid. Let B_i be the ith box, and N_i the number of data points contained in it (subscripts range from 1 to M^2). The conditional probability that a point in B_i goes to B_j on the next iterate is

$$P_{ji} = \frac{\mu(\phi_T^{-1}(B_j) \cap B_i)}{\mu(B_i)}, \tag{10}$$

where μ is the counting measure. Thus, for a given partition, the probability density p_i^n, which gives the probability that the state of the system lies in B_i at iterate n, can be used to determine the probability that the state of the system will lie in B_j at iterate $n+1$ by

$$P_j^{n+1} = P_{ji} p_i^n, \tag{11}$$

where summation is implied by the repeated indices. P_{ji} is a transition probability matrix for the system: note that it depends not only on the system parameters, but also on the partition.

Equation (10) was used to estimate P_{ji} directly *using only the 0th and 1st iterates of the stochastic interrogation data* (i.e., from S and $\phi_T^1(S)$). As one might expect, the statistics in the boxes near the outer edges of S become very poor, and thus the model should not be expected to be very accurate for states in the outer boxes. However, one does expect the asymptotic behavior of the system to be reasonably well approximated, to the level of precision dictated by the partition size, since all data is eventually attracted into the interior of S where the transition probabilities can be computed with reasonably large amounts of data. As a practical matter, care must be taken to choose a partition carefully so that each box has nonzero measure initially. To avoid this problem for the results presented here, we found it convenient to pick our grid to cover an area slightly smaller that the entire set S: an 'overflow' cell was then defined to be the rest of the Poincaré section outside of the gridded area. The cell so constructed provides a well-defined transition probability for any points that either start outside of, or temporarily leave, the gridded region.

Figures 10 and 11 show the results of applying P_{ji} to an initial uniform density on a 30×30 grid (i.e., $p_i^0 = 1/900$ for $1 \leq i \leq 900$). Both figures show the evolution of the 'course-grained' probability density after 1, 2, 3, 4 and 70 iterates of the Poincaré map obtained by repeated application of P_{ji}. The density at 70 iterates is a good approximation to the asymptotic (or 'invariant') density for the system which satisfies $p_i^{n+1} = p_i^n \equiv p_i^*$ (i.e., from equation (11), p_i^* is an eigenvector of P_{ji}). Densities are plotted as surfaces above the zero-phase Poincaré section, with x shown as the horizontal coordinate in all of the plots: each node in the plots is located at the center of the boxes used to construct the model. Figure 10 corresponds to the simple basin data of Figures 5(a), 6(a) and 8(a), whereas Figure 11 corresponds to complicated basin data of Figures 5(d), 6(d), and 8(d).

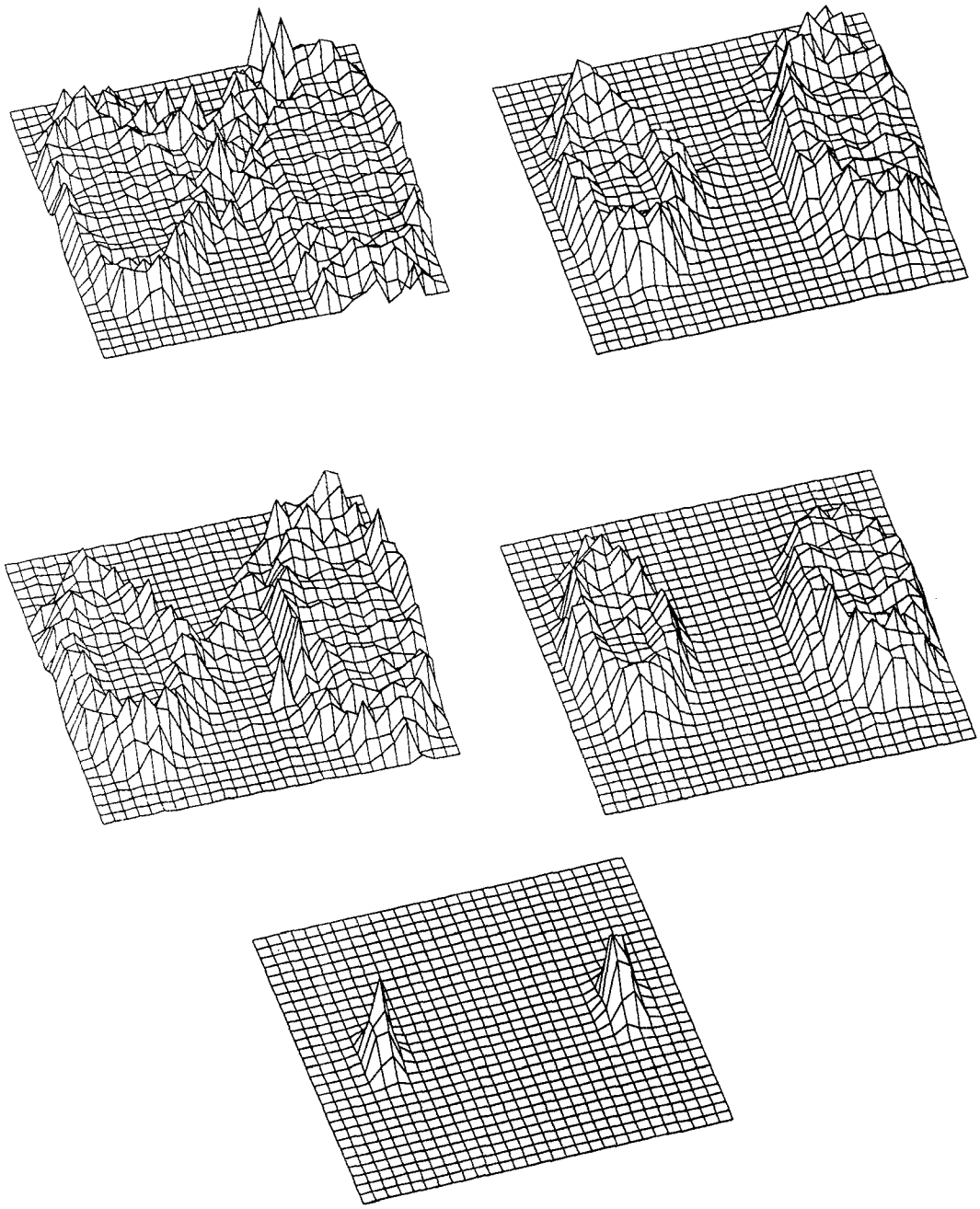

Fig. 10. Evolution of an initially uniform probability density on a 30 × 30 partition of the Poincaré section. The transition probability matrix for the partition, P_{ji}, was constructed using S and $\phi_T^1(S)$ from the $V = 0.098$ V data (Figures 5(a), 6(a), and 8(a)). The plots show the density after 1, 2, 3, 4, and 70 iterates of P_{ji}, with the last plot showing the approximate invariant density. The period-1 orbits are fixed points located near the local maxima of the invariant density.

In the simple basin case of Figure 10, after 4 iterates the density is split into two pieces localized about the attractors, and asymptotically approaches a density in which all of the probability mass is confined to two small regions. The period-1 fixed points of the Poincaré

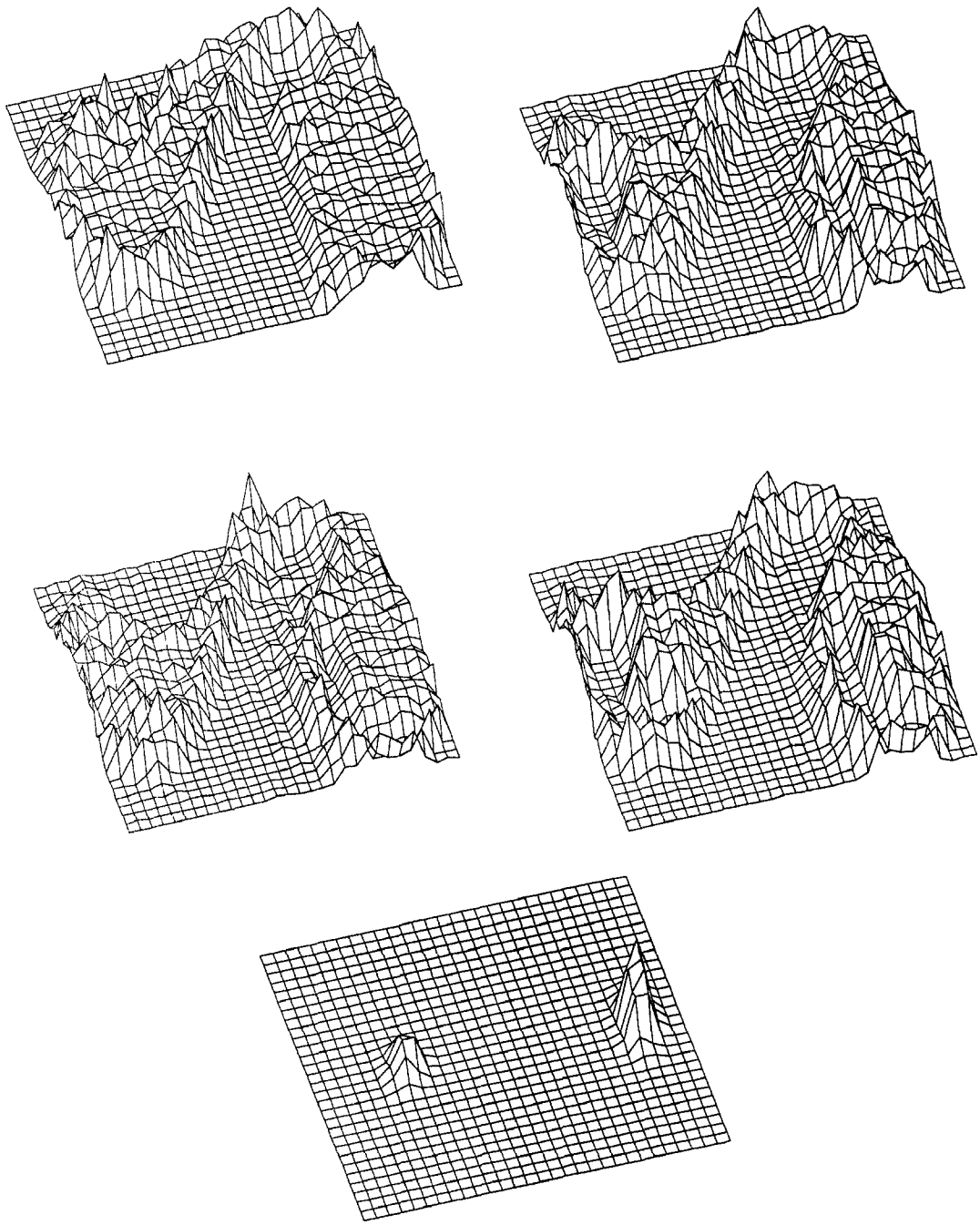

Fig. 11. Same as Figure 10, except the transition probability matrix for the partition was constructed using the V = 0.498 V data (Figures 5(d), 6(d), and 8(d)).

map are located near the peak in each region. In fact, at the grid resolution of the model, these 'local maximum likelihood' points give a best estimate of the fixed-point location. The relative height of each peak in the asymptotic density indicates the relative area of each basin of attraction (limited, of course, to the portion of the Poincaré section for which data was collected). Thus, from Figure 10, one expects the basins to be close to the same size, a fact confirmed by Figure 5(a). The location of the unstable manifold of the saddle-type period-1

orbit is clearly visible in densities corresponding to iterates 2 and 3, thus demonstrating that global features of the system can be studied using the transition probability models.

The complex basin case of Figure 11 shows some marked differences with Figure 10. The greater asymmetry of the global structure of the phase space for this Poincaré sections is readily apparent, even after only the first iterate. This asymmetry continues through to the asymptotic density, which shows that the right basin is roughly twice the size of the left, a fact which, again, is born out by Figure 5(d). Figures 10 and 11 can be thought of as representing an observer's knowledge of the state of the system, starting from a condition of total uncertainty. Thus, Figure 11 demonstrates the way in which homoclinic bifurcation and chaotic transients lead to greater short-term uncertainty in the state of a system: unlike the density of Figure 10, the density of Figure 11 takes significantly longer to become localized near the attractors.

7. Discussion and Conclusions

The stochastic interrogation method described here generates data sets which allow for the experimental visualization and analysis of global features in the phase space of nonlinear oscillators. We have demonstrated the usefulness of this approach by applying it to the study of a driven, two-well nonlinear magneto-mechanical oscillator. The resulting data yielded images of basins of attraction for the system, visualization of the flow of initial states on the Poincaré section, and an estimate of the linear damping coefficient using a novel approach based on Liouville's Theorem.

By combining the basins of attraction with the flow images, we obtained experimental evidence of homoclinic bifurcation well before the onset of chaos. As part of this evidence, a simple-to-complex ('fractal') transition in the basin boundaries was shown to coincide with the appearance of a complicated structure believed to contain the unstable manifold of a saddle-type orbit. This is a significant improvement in experimental technique, since, previously, theoretical criteria for homoclinic bifurcation (such as supplied by the Holmes–Melnikov method) could only be checked by locating regions in the parameter space where chaotic attractors exist. Since homoclinic bifurcation is only a necessary condition for the existence of a chaotic attractor, such studies are typically only able to put loose, one-sided bounds on the theoretical prediction (see, for example, [26]). In principle, our method can check the prediction directly and precisely. Admittedly, for low bandwidth systems, checking a Melnikov curve at more than a few points will be difficult, given the time-consuming nature of the data acquisition task. It is possible, however, that greater sophistication in statistical analysis could lead to accurate predictions with significantly less data. (It should also be pointed out that, of the 35 hours typically needed to collect the basin data, approximately 1/3 was computational overhead required by the specific combination of software, clocks and A/D hardware used for these experiments. This points to an obvious bottleneck which could be improved by better design of the data acquisition system.)

Without question, data collected by stochastic interrogation contains a wealth of dynamical information that the results presented here have barely begun to tap. The estimation of the damping coefficients using Liouville's Theorem and the volume logarithmic decrement promises to be a useful technique because it should be capable of yielding results far away from the equilibria: it is actually a global technique, since there is no assumption of 'small vibrations' in its definition. The main limitation as applied here was the crude volume estimate employed to generate Figure 9. Beyond the determination of basic physical parameters, the stochastic interrogation data contains the information required to construct nonlinear models

of the system. We have used the data to construct transition probability matrices for finite partitions of the phase space, and showed how these matrices allow the evolution of probability densities to be studied. Using only the first few iterates of the data, we were able to obtain significant information concerning the global structure and asymptotic behavior of the system. Current efforts aim at constructing noisy deterministic models using the interrogation data.

Acknowledgements

The work of the first author was supported by the Air Force Office of Scientific Research, and that of the second author by a National Science Foundation Graduate Research Fellowship. The authors have benefitted greatly from discussions with Jim Yorke and Steve Shaw concerning the interpretation of our results, as well as from the constructive criticisms of an anonymous reviewer. The authors would also like to thank Matt Davies for helping them get started with real-time programming. Finally, the assistance of Brian Moquin and Tim Kohler in preparing the color figures was greatly appreciated.

References

1. Moon, F. C. and Holmes, P., 'A magnetoelastic strange attractor', *Journal of Sound and Vibration* **65**(2), 1979, 275–296.
2. Moon, F. C., 'Experiments on chaotic motion of a forced nonlinear oscillator: strange attractors', *ASME Journal of Applied Mechanics* **47**, 1980, 638–644.
3. Testa, J., Perez, J., and Jeffries, C., 'Evidence for universal chaotic behavior of a driven nonlinear oscillator', *Physical Review Letters* **48**(11), 1982, 714–717.
4. Jeffries, C. and Perez, J., 'Direct observation of crises of the chaotic attractor in a nonlinear oscillator', *Physical Review A* **27**(1), 1983, 601–603.
5. Van Buskirk, R. and Jeffries, C., 'Observation of chaotic dynamics of coupled nonlinear oscillators', *Physical Review A* **31**(5), 1985, 3332–3357.
6. Grebogi, C., Ott, E., and Yorke, J. A., 'Fractal basin boundaries, long-lived chaotic transients and unstable–unstable pair bifurcation', *Physical Review Letters* **50**(13), 1983, 935–938.
7. Endo, T. and Chua, L. O., 'Bifurcation diagrams and fractal basin boundaries of phase-locked loop circuits', *IEEE Transactions on Circuits and Systems* **37**(4), 1990, 534–540.
8. Grebogi, C., McDonald, S., Ott, E., and Yorke, J. A., 'Final state sensitivity: an obstruction to predictability', *Physics Letters* **99A**(9), 1983, 416–418.
9. McDonald, S. W., Grebogi, C., Ott, E., and Yorke, J. A., 'Fractal basin boundaries', *Physica* **17D**, 1985, 125–153.
10. Thompson, J. M. T. and Soliman, M. S., 'Fractal control boundaries of driven oscillators and their relevance to safe engineering design', *Proceedings of the Royal Society of London* **428A**, 1990, 1–13.
11. Cusumano, J. P., Lin, D., Morooney, K., and Pepe, L., 'Sensitivity analysis of nonlinear systems using animated basins of attraction', *Journal of Computers in Physics* **6**(6), 1992, 647–655.
12. Guckenheimer, J. and Holmes, P., *Nonlinear Oscillators, Dynamical Systems and Bifurcations of Vector Fields*, Springer-Verlag, New York, 1983.
13. Moon, F. C. and Li, G.-X., 'Fractal basin boundaries and homoclinic orbits for periodic motion in a two-well potential', *Physical Review Letters* **55**(14), 1985, 1439–1442.
14. Yamaguchi, Y. and Mishima, N., 'Fractal basin boundary of a two-dimensional cubic map', *Physical Review Letters* **109A**(5), 1985, 196–200.
15. Grebogi, C., Ott, E., and Yorke, J. A., 'Metamorphoses of basin boundaries in nonlinear dynamical systems', *Physical Review Letters* **56**(10), 1986, 1011–1014.
16. Grebogi, C., Ott, E., and Yorke, J. A., 'Basin boundary metamorphoses: changes in accessible boundary orbits', *Physica* **24D**, 1987, 243–262.
17. Pezeshki, C. and Dowell, E. H., 'An examination of initial condition maps for the sinusoidally excited buckled beam modeled by Duffing's equation', *Journal of Sound and Vibration* **117**(2), 1987, 219–232.
18. Grassberger, P. and Procaccia, I., 'Characterization of strange attractors', *Physical Review Letters* **50**, 1983, 346–349.

19. Mañé, R., 'On the dimension of the compact invariant sets of certain nonlinear maps', *Dynamical Systems and Turbulence*, D. A. Rand and L. S. Young, eds., Springer Lecture Notes in Mathematics, **898**, Springer-Verlag, New York, 1981, pp. 230–242.
20. Grebogi, C., Ott, E., and Yorke, J. A., 'Crises, sudden changes in chaotic attractors, and chaotic transients', *Physica* **7D**, 1983, 181.
21. Arnold, V. I., *Mathematical Methods of Classical Mechanics*, Springer-Verlag, New York, 1978.
22. Meirovitch, L, *Elements of Vibration Analysis*, McGraw-Hill, New York, 1986.
23. Shaw, R., *The Dripping Faucet as a Model Chaotic System*, Aerial Press, Santa Cruz, 1984.
24. Lasota, A. and Mackey, M., *Probabilistic Properties of Deterministic Systems*, Cambridge University Press, Cambridge, 1985.
25. Hsu, C. S., *Cell-to-Cell Mapping, a Method of Global Analysis for Nonlinear Systems*, Springer-Verlag, New York, 1987.
26. Moon, F. C., Cusumano, J. P., and Holmes, P. J., 'Evidence for homoclinic orbits as a precursor to chaos in a magnetic pendulum', *Physica* **24D**, 383–390.